Chapter 7

Experiment environment and detector designs

Two complementary detector designs, the "CLIC-like Detector" (CLD) and the "International Detector for Electron-positron Accelarators" (IDEA), are being studied for the FCC-ee. Before outlining these two concepts in Sections 7.3 and 7.4, respectively, aspects common to the two detectors are presented, namely a description of the experimental environment including an estimate of beam-induced background levels in Section 7.1, and the measurement of luminosity in Section 7.2. The detector magnet systems, the constraints on the readout, and the infrastructure requirements are discussed in Sections 7.5, 7.6, and 7.7.

7.1 Experiment Environment

The colliding electron and positron beams of the FCC-ee cross with an angle of 30 mrad at two interaction points (IP). A detector is placed at each IP, with a solenoid that delivers a magnetic field parallel to the bisector of the two beam axes, called the z axis. The two beam directions define the (x, z) horizontal plane (Fig. 7.1). Each beam therefore traverses the axial magnetic field from the detector solenoid at an angle of 15 mrad, which imposes an upper limit of 2 T on the field strength. In order to preserve the beam emittance, and thus a high luminosity, it is necessary to place a set of two compensating solenoids around the beam line just in front of the final focussing quadrupoles (Section 2.5.2). The compensating solenoids intrude into the detector to a distance $z \simeq \pm 1.20$ m from the IP. All machine elements, including the compensating solenoids, are kept inside a cone with an opening angle of 100 mrad about the z axis. The cylindrical central part of the beam pipe, which fully covers the angular range down to 150 mrad in front of the tracking detectors, has an inner radius of 15 mm and a total thickness of 1.7 mm, made up of 1.2 mm of beryllium, cooled by a 0.5 mm layer of water. At normal incidence, this material corresponds to 0.47% of a radiation length (X_0).

The time between two bunch crossings (BX) varies from a minimum of 20 ns at the Z pole to a maximum of 7 µs at the highest energy, $\sqrt{s} = 365$ GeV. The unprecedented luminosity – 10^5 times that delivered by LEP at the Z pole – brings challenges in controlling the impact of various beam-induced backgrounds (synchrotron radiation, photon-photon collisions, beam-gas interactions) on the detector performance.

7.1.1 Synchrotron Radiation

Synchrotron radiation (SR) [200] sets constraints on the asymmetric design of the interaction region (Section 2.5.4). As shown in Fig. 2.12, an appropriate set of tungsten masks needs to be added in front of the final focus quadrupoles to protect the interaction region from direct hits of SR photons from the last bending magnet. The number of SR photons that scatter from the masks to the detector volume increases strongly with beam energy (Table 2.7). Bringing this background to a tolerable level at the highest energy therefore ensures that it becomes negligible at lower energies.

These masks (in orange in Fig. 2.12) are placed inside the beam pipe, at the exit of the final focus quadrupoles (QC1), about 2.1 m from the IP. To further limit the fraction of the SR fan that scatters off the masks and showers into the detector area, an ingenious shielding scheme has been developed to minimise the impact on the detector performance. Tungsten shields (in turquoise blue) are positioned outside the beam pipe. A requirement for the position of the shield comes from the need to leave the acceptance window in front of the luminometers (in magenta) unshielded, from 50 to 100 mrad around the outgoing beams. This constraint results in an asymmetric azimuthal coverage of the shielding material around the beam pipe in the luminometer acceptance window, $330 < |z| < 1191.4$ mm, which leaves the vertex detector partially unshielded against SR. Figure 7.1 shows the implementation of the shield in the GEANT4 detector model used for background simulation studies. The thickness of the shield up to the rear end of the luminometer, $|z| < 1191.4$ mm, is limited to 0.1 mm, whereas it becomes 15 mm with full coverage of the two beam pipes from the rear end of the luminometer up to QC1.

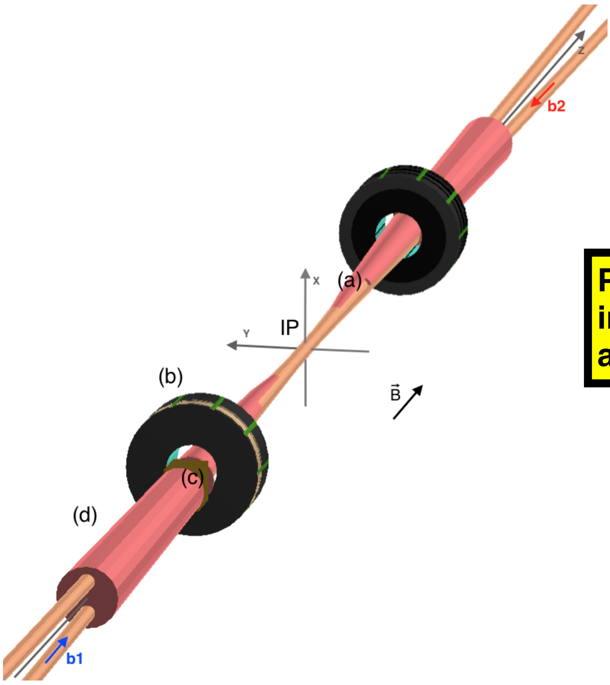

Possible to rotate to not interchange horizontal and vertical directions?

Figure 7.1: Sketch of the implementation of the interaction region in GEANT4. The tungsten shielding of the beam pipe appears in pink. The shielding from 330 mm (a) to the rear of the luminometer at 1191.4 mm (b) is 0.1 mm thick and covers only a 68° azimuthal wedge on the positive-x side of the beam pipe. Further back, a full 15 mm thick tungsten cone covers both beam pipes to protect the tracking detectors from synchrotron radiation. To get a better rendering, the horizontal (x, z) plane was rotated by 90 degrees around the z axis.

Photons from the last bend scatter on the lower mask and partially forward-scatter into the detector area. The forward-scattered photons were simulated with SYNC_BKG [272] and it was found that the distribution of their energies, with peaks at 70 keV and 250 keV, does not exceed 1 MeV. The photon interactions were modelled in a full GEANT4 [273] simulation that includes the interaction region with or without beam-pipe shielding, the luminometer (Section 7.2), and the CLD detector model (Section 7.3). While no hits are produced in the whole tracker volume at lower energies, a few hits (164 per BX) are observed at $\sqrt{s} = 240$ GeV, and most (6.6×10^{4} per BX) at $\sqrt{s} = 365$ GeV. These numbers reduce 2.5 (700) hits per BX with the proposed shield in place. With this appropriate shielding, the effect of the SR on the detector is thus not expected to be an issue. More details are given in Section 7.3.2.

7.1.2 Pair-Production Background

With the extreme FCC-ee luminosities, the production of low-energy e^+e^- pairs from photon-photon collisions becomes a significant source of background, in particular in detector elements close to the beam pipe. At the FCC-ee, the dominant production mode is incoherent pair creation (IPC), whereby the e^+e^- pairs are produced in interactions involving virtual or real photons from beamstrahlung. The GuineaPig++ [163] event generator was used to study this background at $\sqrt{s} = 91.2$ and 365 GeV. Table 7.1 summarises the $e^\pm$ production rates at both centre-of-mass energies, together with their total energy. The table also shows the rates of particles that eventually enter the CLD vertex detector acceptance. While a large number of particles is created, only those that are emitted with a significant angle, θ, with respect to the z-axis and momentum transverse to that axis (p_{T}), enter the detector volume. The others remain trapped around the axial magnetic field lines from the detector solenoid.

Table 7.1: Total numbers of $e^\pm$ created per BX by incoherent pair production, their total energy, and the rates of these particles that would reach the CLD vertex detector within a magnetic field of 2 T. Numbers are obtained from GuineaPig, prior to any detector simulation.

$\sqrt{s}$ [GeV]	91.2	365
Total particles	800	6200
Total E (GeV)	500	9250
Particles with $p_{\mathrm{T}} \geq 5\,\mathrm{MeV}$ and $\theta \geq 8^\circ$	6	290

The kinematics of the $e^\pm$ produced with $E > 5$ MeV is illustrated in Fig. 7.2. The peak of particle flux seen at $\theta \sim 15$ mrad corresponds to particles emitted close to the direction of the outgoing beams. The dense region at higher θ corresponds to e^- (e^+) particles that are emitted in the direction of the outgoing e^+ (e^-) beam and that are deflected towards larger polar angles by the electromagnetic field of the bunch. With a magnetic field of 2 T, only the particles produced with $p_{\mathrm{T}} > 5$ MeV would reach the first layer of the CLD vertex detector, within its angular acceptance $\theta > 8^\circ$. The numbers given in Table 7.1 indicate that this background is rather moderate. More details are given in Section 7.3.2.

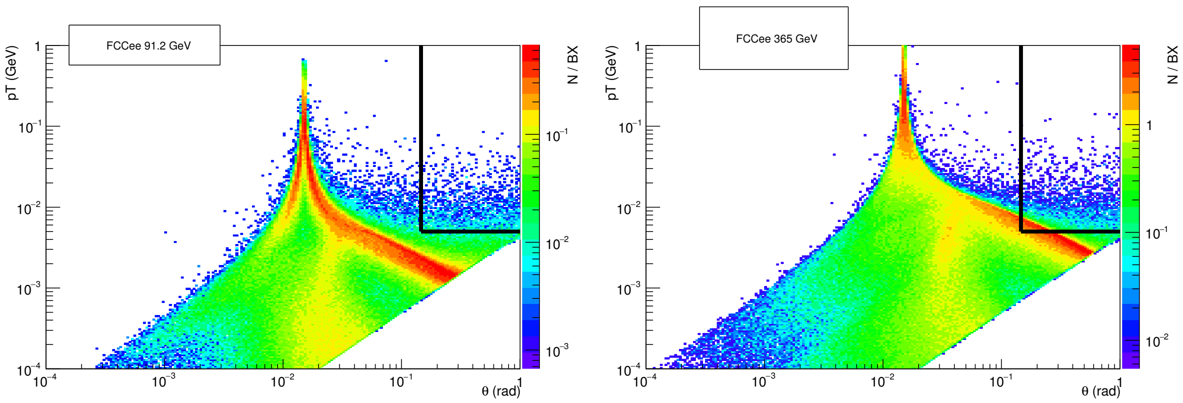

Figure 7.2: Rates of $e^\pm$ from IPC in the (p_{T}, θ) plane, in the detector frame, for $\sqrt{s} = 91.2$ GeV (left) and 365 GeV (right). The black line in the upper-right corner delineates the CLD vertex detector acceptance within a field of 2 T.

Photon-photon collisions can also give rise to hadrons, possibly resulting in jets piling-up in the detector. These interactions were simulated with a combination of GuineaPig and Pythia6 [274]. Less than 10^{-3} (10^{-2}) events are produced per BX at $\sqrt{s} = 91.2$ (365) GeV with an invariant mass of the $\gamma\gamma$ system in excess of 2 GeV. This background was therefore found to be negligible.

7.2 The Luminometer

For the cross-section measurement, an accurate knowledge of the integrated luminosity is required. The potential precision of the Z lineshape determination (Section 1.2) sets the goal for the *absolute* luminosity measurement to a precision of 10^{-4}. The *relative* luminosity between energy scan points must also be controlled to better than 5×10^{-5}. The former requirement is the most challenging because many sources of systematic uncertainty contributing to the absolute luminosity measurement, including that from the geometrical definition of the detector acceptance, cancel for the relative luminosity measurement.

Due to its large cross section, of the same order as the Z production cross section at the Z pole, the reference process for the luminosity measurement is small angle Bhabha scattering $e^+e^- \rightarrow e^+e^-$. This process may also be complemented by the large angle $e^+e^- \rightarrow \gamma\gamma$ production. In spite of a cross section several orders of magnitude smaller, this process statistically suffices to reach and exceed an absolute precision of 10^{-4} at the Z pole in the FCC-ee luminosity conditions, and enjoys entirely different sources of systematic uncertainties. More studies are needed to prove the reliability of this alternative measurement. This section therefore describes only the detector and the methodology for luminosity measurement with small angle Bhabha scattering.

7.2.1 Luminometer Design

Based on the experience from LEP [275, 276] and on linear collider studies [277, 278], the luminometer consists of a pair of small angle calorimeters made of silicon-tungsten layers. The calorimeters are centred around – and tilted to be perpendicular to – the outgoing beams to measure the scattering angle of the elastically scattered electrons and positrons precisely. The space available for the luminometers is severely constrained. The compensating solenoids, extending to $z \simeq \pm 1.2$ m, push the luminometers far into the detector volume. At their inner radius, the luminometers have to stay clear of the incoming beam pipe. At their outer radius, they must not interfere with the forward coverage of the tracking detectors and therefore must stay fully inside a cone of 150 mrad around the main detector axis of symmetry. The proposed luminometer design is shown in Fig. 7.3. The mechanical inner (outer) radius is 54 (145) mm. The sensitive region, instrumented with silicon sensors, extends from 55 to 115 mm. The calorimeters consist of 25 layers, with each layer comprising a 3.5 mm tungsten plate, equivalent to 1 X_0 and a silicon sensor plane inserted in the 1 mm gap. In the transverse plane, the silicon sensors are finely partitioned into pads. The proposed number of divisions is 32 both radially and azimuthally for 1 024 readout channels per layer, or 25 600 channels in total for each calorimeter. The calorimeter sandwich extends along the outgoing beam axis between 1074 mm and 1190 mm from the interaction point. The inactive region with radii between 115 and 145 mm is used for services, which include the mechanical assembly of the tungsten-silicon sandwich, front-end electronics, cables, cooling and equipment for mechanical alignment.

Each calorimeter is divided vertically into two half barrels clamped together around the beam pipe. The calorimeters have a weight of about 65 kg each. Due to the compactness of the devices it is possible to produce each silicon half-layer from a single silicon tile, which minimises potential inactive regions between sensors and facilitates precise geometrical control of the acceptance. Meticulous care is required for the design of the vertical assembly of the two half-barrels, both in order to avoid a non-instrumented region and for the precise control of the geometry. In order to decouple the luminometers mechanically from the magnetic elements of the collider, it is being considered to fix the beam pipe to the luminometers, and the luminometers to a support tube connected to the end-cap calorimeter system.

The silicon sensor pads are connected to the compact front-end electronics positioned at radii immediately outside the sensors. To limit the high detector occupancy to manageable levels, it is desirable

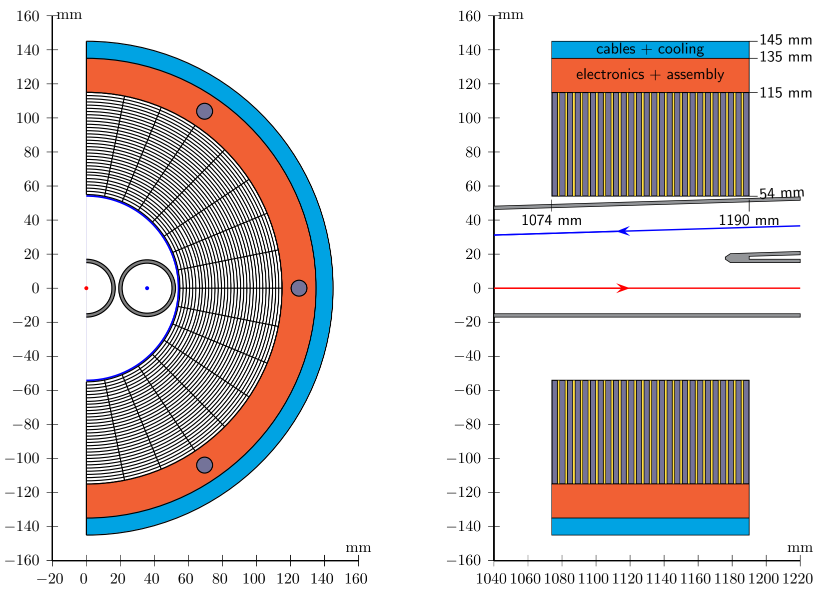

Figure 7.3: The luminosity calorimeter centred around the outgoing beam line: front view (left), top view (right).

to read out the detector for each bunch crossing, which calls for the development of readout electronics with a shaping time shorter than 20 ns. A power budget of 5 mW per readout channel is estimated, for a total of 130 W per calorimeter, which has to be removed by cooling. In order to maintain the geometrical stability required (Section 7.2.2), the temperature of the luminometers must be kept stable and uniform within ± 1K or better.

7.2.2 Acceptance and Luminosity Measurement

The SiW sandwich has an effective Molière radius of about 15 mm. For a robust energy measurement, the fiducial acceptance limits are kept about one Moliere radius away from the borders of the instrumented area, effectively limiting the acceptance to the 62–88 mrad range. To ensure that the luminosity measurement depends only to second order on possible misalignments and movements of the beam spot relative to the luminometer system, the method of asymmetric acceptance [279] is to be employed. Bhabha events are selected if the $e^{\pm}$ is inside a narrow acceptance in one calorimeter, and the $e^{\mp}$ is inside a wide acceptance in the other. A 2 mrad difference between the wide and narrow acceptances is deemed adequate to accommodate possible misalignments. The narrow acceptance thus covers the angular range 64–86 mrad, corresponding to a Bhabha cross section of 14 nb at the Z pole (to be compared to 40 nb for Z production), equivalent to 6.4×10^{-4} events per bunch crossing.

The forward-peaked $1/\theta^3$ spectrum of the Bhabha scattering process causes the luminosity measurement to be particularly sensitive to the determination of this angular range. The Bhabha acceptance A, and therefore the luminosity, is indeed affected by any change $\Delta R_{\rm in}$ ($\Delta R_{\rm out}$) of the inner (outer) edge radial coordinate as follows: $\Delta A/A \approx -(\Delta R_{\rm in}/1.6\,\mu{\rm m}) \times 10^{-4}$ and $\Delta A/A \approx +(\Delta R_{\rm out}/3.8\,\mu{\rm m}) \times 10^{-4}$. Similarly, A is affected by any change ΔZ of the half-distance between the effective planes of the radial measurements in the two calorimeters: $\Delta A/A \approx +(\Delta Z/55\,\mu{\rm m}) \times 10^{-4}$. With the 30 mrad beam crossing angle, the two calorimeters are centred on different axes, and Z should then be interpreted as $Z = \frac{1}{2}(Z_1 + Z_2)$, where Z_1 and Z_2 are the two distances, measured along the two outgoing beam directions, from the (nominal) IP to the luminometers.

With the method of asymmetric acceptance, only a weak, second-order, dependence of the acceptance remains on the IP position. The size of this effect was investigated through a high-statistics study of a Bhabha event sample generated with the event generator BHLUMI [280]. The study, based on a parameterised detector response, confirmed the second order dependence as long as shifts of the IP are small enough to be covered by the difference between the wide and narrow acceptance definitions: in this case, up to shifts of about $\delta r = 0.5$ mm transversely and $\delta z = 20$ mm longitudinally. Inside this range, the changes of the acceptance observed could be parameterised as $\Delta A/A \approx +(\delta r/0.6\,\text{mm})^2 \times 10^{-4}$ and $\Delta A/A \approx -(\delta z/6\,\text{mm})^2 \times 10^{-4}$. It should be noted that such shifts of the IP position give rise to asymmetries in the Bhabha counting rate either azimuthally (radial shift) or between the two calorimeters (longitudinal shifts) and can thus be monitored and corrected for directly from the data. No such possibility of correction from the data is present for the detector construction tolerances, ΔR and ΔZ, discussed in the previous paragraph, which therefore need to be monitored with an independent alignment device.

In summary, to reach a precison of 10^{-4} on the absolute luminosity measurement, the radial dimensions of the luminometers have to be controlled to the one micron level, whereas the distance between the two luminometers has to be controlled to about 100 µm. The requirements on the alignment of the luminometer system with respect to the interaction point position are considerably more relaxed: accuracies of order 0.1 mm and 1 mm are called for in the radial and longitudinal directions, respectively.

7.2.3 Electromagnetic Focussing of Bhabha Electrons

The final state $e^{\pm}$ from Bhabha scattering are focussed [281] by the strong electromagnetic field of the opposing bunch in the same way as the beam particles. The effect and its mitigation are being studied with events generated by `BHWIDE` [282] and injected into GuineaPig++ [163], which then tracks the final state particles to the outside from a randomly chosen scattering point within the collision diamond.

Early results indicate an average focussing of the final state $e^{\pm}$ in the luminometer region of about 40 µm corresponding to a relative decrease in acceptance of about 20×10^{-4}. The focussing is most pronounced in the positive x direction, i.e. for the tracks closest to the outgoing beam direction. This azimuthal asymmetry is found to strongly correlated to the magnitude of the focussing effect. Studies are being performed to show that the direct measurement of this asymmetry can be used to correct the induced bias on the luminosity.

Update with results of Yorgos' studies

7.2.4 Machine and Beam-induced Backgrounds in the Luminometer

A full simulation of the impact of IPC on the luminometers was performed for $\sqrt{s} = 91.2$ GeV, where the requirements for the precision of the luminosity measurement are the strongest. The total energy deposited by IPC pairs in each calorimeter is only 350 MeV per bunch crossing. The calorimeter cells that see the largest energy deposits are at the lowest radii and at the rear of the calorimeter, thus outside the fiducial volume relevant for the luminosity measurement. Consequently, the IPC background is not expected to compromise the precision of the luminosity measurement. In any case, it was verified that this background could be eliminated by placing a thin layer of tungsten shielding at the inner radius of the luminometers.

The total energy released per BX by synchrotron radiation in each luminosity calorimeter at $\sqrt{s} = 365$ GeV (where the effect of SR is largest) was found to be reduced from 340 MeV without shielding to only 7 MeV with the proposed beam-pipe shield, without any significant effect on the performance of the luminometer.

At LEP, the primary source of background for the luminosity measurement was from off-momentum particles generated by beam scattering with the residual gas in the beam pipe, in the straight sections before the experiments, and deflected by the quadrupoles into the luminometers [275]. Early studies [283] of beam-gas interactions at FCC-ee were performed, for $\sqrt{s} = 91.2\,\text{GeV}$, with a vacuum of 10^{-9} mbar of N_2 at 300 K. The studies demonstrate an induced rate of particles leaving the beam pipe of 140 kHz per meter per beam in the region close to the IP. It was found that only a small fraction of these particles are deflected sufficiently by the quadrupoles to point towards the opposite side luminosity calorimeter, and that most of those that do point there will be effectively stopped by the tungsten shielding around the beam pipe. The remaining small number of particles that enter the luminometer have low energy, typically less than half the beam energy. The coincidence rate between the two calorimeters caused by beam-gas interaction was found to be more than two orders of magnitude below the Bhabha rate. This observation puts the FCC-ee in a favourable situation with respect to LEP, where the two rates were comparable at this point. Energy and angular requirements, which were able to considerably reduce the LEP coincidence rate, bring this background down to a negligible level at the FCC-ee.

7.3 The CLD Detector Design

The CLD detector has been adapted to the FCC-ee specificities from the most recent CLIC detector model [284], which features a silicon pixel vertex detector and a silicon tracker, followed by highly granular calorimeters (a silicon-tungsten ECAL and a scintillator-steel HCAL). A superconducting solenoid provides a 2 T magnetic field, and a steel yoke interleaved with resistive plate muon chambers (RPC) closes the field.

To compensate for the lower field strength, the tracker radius was enlarged from 1.5 to 2.1 m. The HCAL depth was reduced from 7.5 to 5.5 nuclear interaction lengths (λ_I) to profit from the lower centre-of-mass energy. Another difference with respect to CLIC stems from the continuous operation of a circular collider, which hinders the use of power pulsing for the electronics. The impact on cooling and material depends on technology choices and therefore detailed engineering studies on cooling systems are needed. Based on the developments for the ALICE inner tracking system upgrade (ITS) [285], the amount of material per layer for the vertex detector has been increased by a factor 1.5 with respect to the CLIC vertex detector.

A comparison of the main parameters in the CLD concept and the CLIC detector model is presented in Table 7.2. The CLD concept is illustrated in Fig. 7.4.

Table 7.2: Comparison of key parameters of CLD and CLIC detector models.

Concept	CLICdet	CLD
Vertex inner radius [mm]	31	17
Tracker half length [m]	2.2	2.2
Tracker outer radius [m]	1.5	2.1
ECAL absorber	W	W
ECAL X_0	22	22
HCAL absorber	Fe	Fe
HCAL λ_I	7.5	5.5
Solenoid field [T]	4	2
Overall height [m]	12.9	12.0
Overall length [m]	11.4	10.6

7.3.1 CLD Tracking System

The CLD vertex detector (VXD) consists of a cylindrical barrel closed off in the forward directions by disks. The layout is based on double layers, made of two sensitive layers fixed on a common support structure, which includes cooling circuits. The barrel consists of three double layers and the forward region is covered by three sets of double disks.

The CLD concept features an all-silicon tracker. Engineering and maintenance considerations led to a design with a main support tube for the inner tracker region including the vertex detector. The inner tracker (IT) consists of three barrel layers and seven forward disks. The outer tracker (OT) completes the

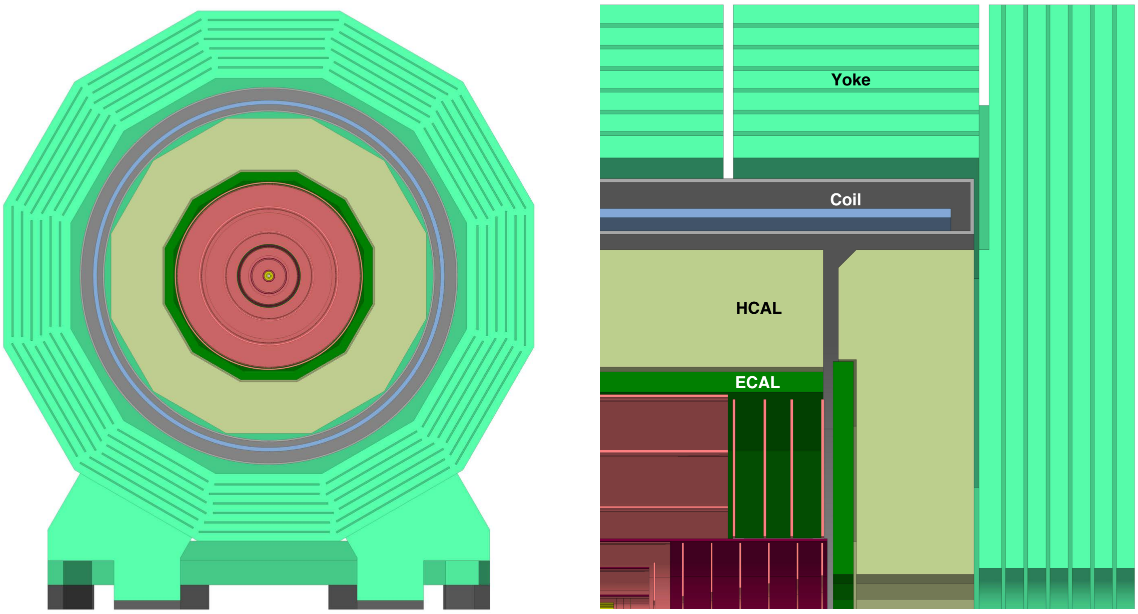

Figure 7.4: The CLD concept detector: end view cut through (left), longitudinal cross section of the top right quadrant (right).

system with an additional three barrel layers and four disks. The overall geometrical parameters of the tracker are given in Table 7.2.

Preliminary engineering studies have been performed for the CLIC detector to define the support structures, cooling systems, etc. needed for the tracker barrel layers and disks. For the outer tracker barrel support, these studies were completed by building and testing a prototype. The same concepts and material thicknesses are currently used for CLD. The additional material needed for the 200 µm thick layer of silicon including the extra support structures, cables and cooling infrastructure has been estimated. The total material amounts to about $11\%(20\%)X_0$ in the barrel (forward) region.

Full simulation studies have been carried out in order to assess the performance of the CLD tracker. The single-point resolutions for each sub-detector elements were assumed to be 3×3 µm^2 for the vertex detector; 5×5 µm^2 for the inner-most layer of the inner tracker; and 7×90 µm^2 for the other layers of the inner tracker and the outer tracker. The momentum resolution obtained for muons is shown in Fig. 7.5. For high momentum muons in the central region, a resolution of $\Delta\,(1/p_{\mathrm{T}}) < 5\times 10^{-5}$ GeV^{-1} is achieved. The study showed a tracking efficiency of 100% for single muons with a transverse momentum above 1 GeV. The efficiency also remains high for softer muons, falling off gradually to reach about 96% for $p_{\mathrm{T}} = 0.1$ GeV. The tracking efficiency for particles in busier environments was studied with light-quark pair events at $\sqrt{s} = 91$ and 365 GeV. A tracking efficiency of almost 100% was found whenever $p_{\mathrm{T}} > 1$ GeV.

7.3.2 Backgrounds in the CLD Tracking System

The effect of IPC and SR backgrounds on the CLD tracker performance has been studied through a full GEANT4 simulation of the interaction region and the CLD detector. The simulation used `DD4hep` [286], and the `ddsim` software framework developed by the CLIC-dp collaboration. Hits with an energy deposit above a threshold of a few keV in the silicon sensors are assumed to be recorded. When occupancies are determined, the numbers of such hits are multiplied by an average cluster size, chosen to be 5 (2.5) for the pixel (strip) sensors, and by a safety factor of three. A pitch of 25×25 µm^2 was taken for the pixels of the vertex detector and of 1×0.05 mm^2 for the strips of the inner and outer tracker.

The IPC background cause on average about 50 (1100) hits per BX in the VXD, at $\sqrt{s}$ =

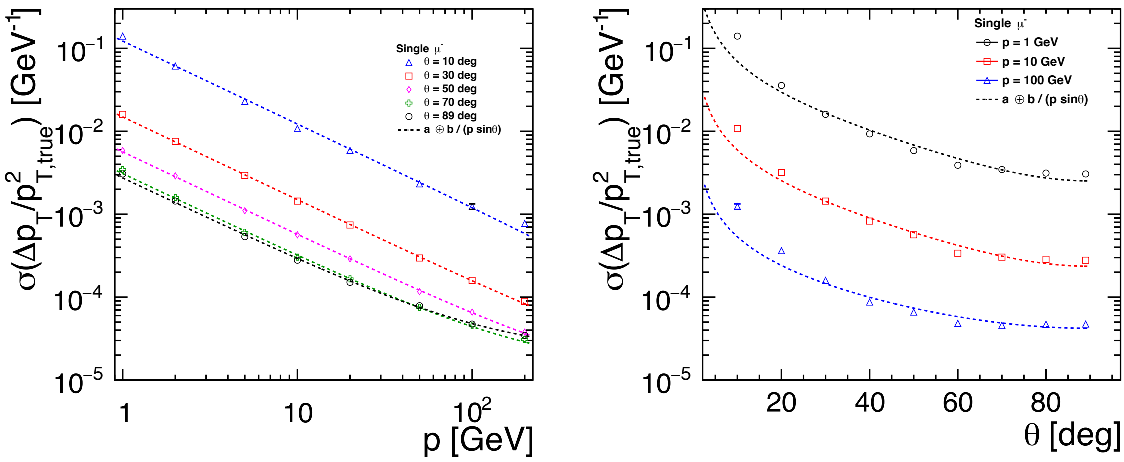

Figure 7.5: Transverse momentum resolution for single muons as a function of momentum at fixed polar angle θ = 10, 30, 50 70 and 89 degrees (left), and as a function of polar angle at fixed momentum p = 1, 10 and 100 GeV (right).

91.2 (365) GeV. The occupancy is highest in the innermost barrel layer of the VXD, on average reaching 7×10^{-6} (1.5×10^{-4}) per BX. The peak occupancy reaches 1×10^{-5} (4×10^{-4}) at the edges of the VXD barrel ladders, and about half these values for low radii of VXD end-caps. As an illustration, Fig. 7.6 shows the hit density in the VXD at $\sqrt{s}$ = 365 GeV. The highest hit density in the tracker is observed at

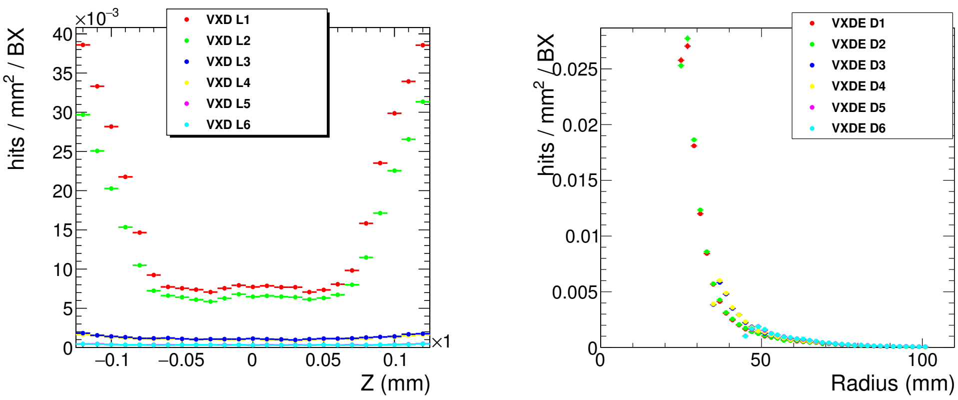

Figure 7.6: Hit density per BX in the CLD VXD induced by the IPC background at $\sqrt{s}$ = 365 GeV; barrel layers (left), endcap disks (right).

the inner radii of the first disk. The induced occupancy is 2×10^{-5} (1×10^{-4}) per BX. When operating at the Z pole, where two consecutive bunch crossings are separated by 20 ns, the readout electronics is likely to integrate the deposited charge over several BXs. Even with a “slow” readout electronics integrating over 1 μs (50 BXs), the maximum occupancy observed would remain below 10^{-3}. In summary, detector occupancies induced by IPC backgrounds are not expected to affect the tracking performance.

As discussed in Section 7.1, synchrotron radiation in the detector volume is negligible at all energies except the top energy. At this energy, the resulting large number of hits (∼60,000 per BX) in the inner and outer tracking detectors without shielding is very effectively reduced to a negligible level by the tungsten shielding of the beam pipe. The shielding does not fully protect the vertex detector, however, where a total of about 350 hits per BX would be created, mostly in the first and second double layers. The maximum occupancy is of order of 10^{-4}, and is not expected to affect the tracking performance.

7.3.3 CLD Calorimetry

Studies in the context of linear colliders have concluded that high-granularity calorimetry associated with a silicon tracker may be an option to reach a jet energy resolution of $\sim 4\%$ with particle-flow reconstruction. In contrast to a purely calorimetric measurement, particle-flow reconstruction enables the identification and the reconstruction of all visible particles in an event [287,288]. An overview of the CLD particle-flow reconstruction and the associated Pandora PFA software can be found in Ref. [289]. Experimental tests are described in Ref. [290].

An ECAL segmentation of $5 \times 5\ \mathrm{mm}^2$ is deemed adequate to resolve energy deposits from nearby particles in jets. The technology chosen as baseline option is a silicon-tungsten sandwich structure. In order to limit the leakage beyond the ECAL, a total depth of around 22 X_0 was chosen. A longitudinal segmentation with 40 identical Si-W layers was found to give the best photon energy resolution. A full simulation study with the Pandora PFA reconstruction has been performed for single photons with energies between 10 and 100 GeV. The resulting photon energy resolution is shown in Fig. 7.7.

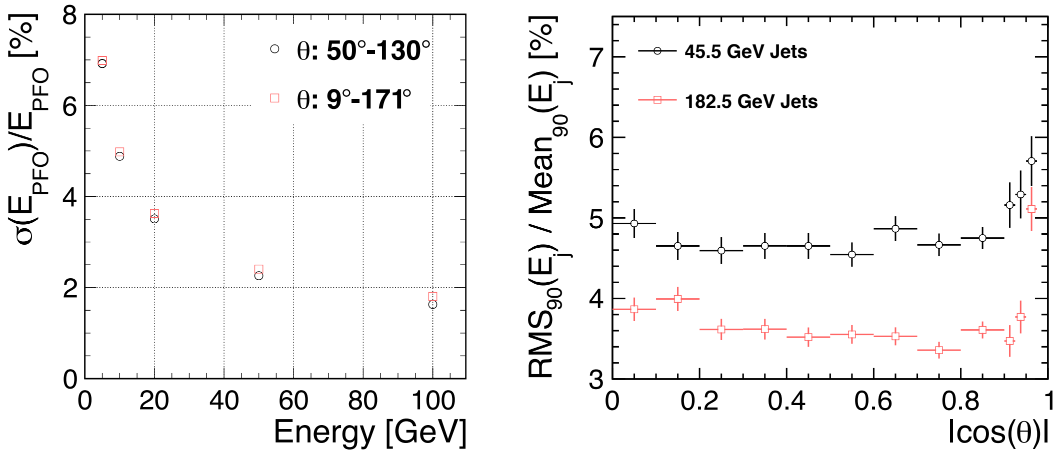

Figure 7.7: CLD calorimeter performance. Photon energy resolution as a function of energy (left), comparing the barrel region with the full detector acceptance. Jet energy resolution for light quark jets as a function of polar angle (right).

The hadron calorimeter is made of steel absorber plates, each 19 mm thick, interleaved with scintillator tiles. The polystyrene scintillator, in a steel cassette, is 3 mm thick with a tile size of $30\times$ 30 mm^2. Analogue readout of the tiles with SiPMs (silicon photomultipliers) is envisioned. The HCAL consists of 44 layers and is around 5.5 λ_I deep, which brings the combined thickness of ECAL and HCAL to 6.5 λ_I. A study of the CLD performance with the Pandora PFA reconstruction was carried out with light-quark pair events at $\sqrt{s} = 91.2$ and 365 GeV. Figure 7.7 shows the jet energy resolution obtained as a function of polar angle.

7.3.4 CLD Muon System

The CLD muon system comprises six detection layers with an additional seventh layer in the barrel immediately following the coil. The latter may serve as a tail catcher for energetic hadron showers. The detection layers are proposed to be built as RPCs with cells of $30\times$ 30 mm^2. (Alternatively, crossed scintillator bars could be envisioned.) The yoke layers and thus the muon detectors are staggered to avoid non-instrumented gaps.

7.4 The IDEA Detector Concept

The IDEA detector concept, developed specifically for FCC-ee, is based on established technologies resulting from years of R&D. Additional work is, however, needed to finalise and optimise the design. The structure of the IDEA detector is outlined in Fig. 7.8, and its key parameters are listed in Table 7.3. The detector comprises a silicon pixel vertex detector, a large-volume extremely-light short-drift wire chamber surrounded by a layer of silicon micro-strip detectors, a thin, low-mass superconducting solenoid coil, a pre-shower detector, a dual-readout calorimeter, and muon chambers inside the magnet return yoke.

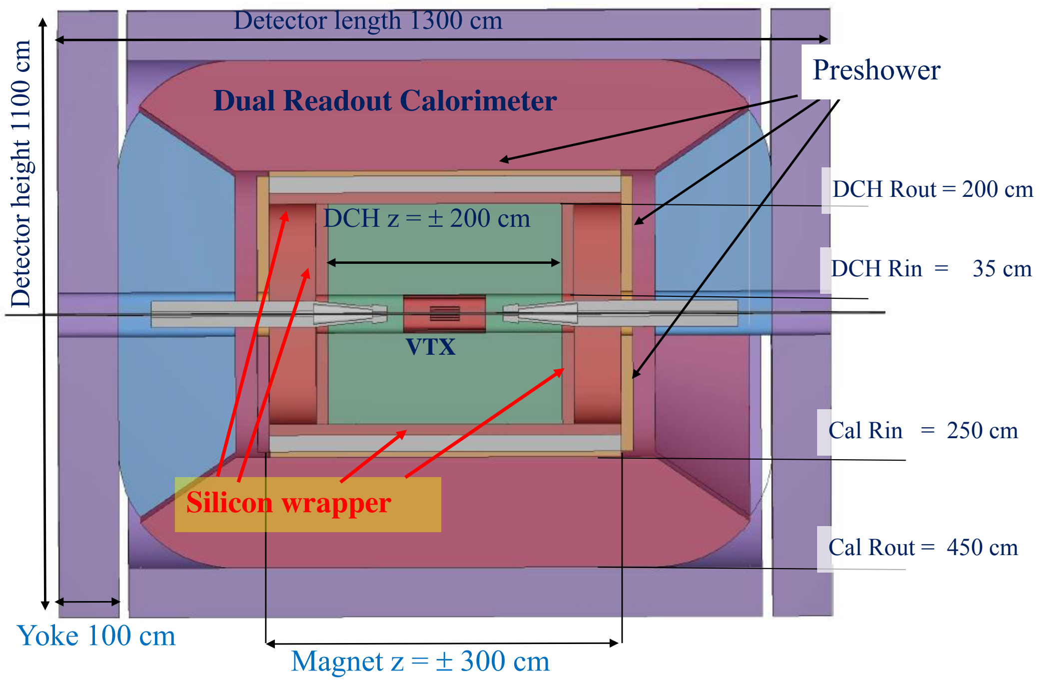

Figure 7.8: Schematic layout of the IDEA detector.

Table 7.3: Key parameters of the IDEA detector.

Vertex technology	silicon
Vertex inner / outer radius	1.7 cm / 34 cm
Tracker technology	Drift Chamber + Silicon Wrapper
Tracker half length / outer radius	2.0 m / 2.0 m
Solenoid bore radius / half length	2.1 m / 3.0 m
Preshower / calorimeter absorber	lead / lead
Preshower inner / outer radius	2.4 m / 2.5 m
DR calorimeter inner / outer radius	2.5 m / 4.5 m
Overall height / length	11 m / 13 m

7.4.1 IDEA Vertex Detector

The innermost detector, surrounding the beam pipe, is a silicon pixel detector. Recent test-beam results on the detectors planned for the ALICE ITS upgrade, based on the ALPIDE readout chip [291], indicate an excellent ($\sim$ 5 µm) resolution, high efficiency at low power, and low dark-noise rate [292]. These very light detectors, 0.3–1.0% X_0 per layer, are the basis for the IDEA vertex detector.

7.4.2 IDEA Drift Chamber

The drift chamber (DCH) is designed to provide good tracking, high-precision momentum measurement and excellent particle identification by cluster counting. The main peculiarity of this chamber is its high transparency, in terms of radiation lengths, obtained as a result of the novel approach adopted for the wiring and assembly procedures [293]. The total amount of material in the radial direction towards the barrel calorimeter is of the order of 1.6% X_0, whereas, in the forward direction, it is about 5.0% X_0, 75% of which are in the end-plates instrumented with the front-end electronics. The original ancestor of the DCH design is the drift chamber of the KLOE experiment [294], which was more recently developed as the MEG2 [295] drift chamber.

The DCH is a unique-volume, high-granularity, all-stereo, low-mass, cylindrical, short-drift, wire chamber, co-axial with the 2 T solenoid field. It extends from an inner radius $R_{\text{in}} = 0.35$ m to an outer radius $R_{\text{out}} = 2$ m, for a length L = 4 m and consists of 112 co-axial layers, at alternating-sign stereo angles, arranged in 24 identical azimuthal sectors. The square cell size varies between 12.0 and 14.5 mm for a total of 56 448 drift cells. The challenges potentially arising from large number of wires are addressed by the peculiar design of the wiring successfully employed for the recent construction of the MEG2 drift chamber [296]. The chamber is operated with a very light gas mixture, 90% He – 10% iC_4H_{10} (isobutane), corresponding to a maximum drift of $\sim$ 400 ns. The number of ionisation clusters generated by a minimum ionising particle (m.i.p.) is about 12.5 cm^{-1}, allowing cluster counting/timing techniques to be employed to improve both spatial resolution (σ_x < 100 µm) and particle identification ($\sigma(dN_{\text{cl}}/dx)/(dN_{\text{cl}}/dx) \approx 2\%$). The angular coverage extends down to $\sim$13°, and could be further extended with additional silicon disks between the DCH and the calorimeter end-caps.

A drift distance resolution of 100 µm has been obtained in a MEG2 drift chamber prototype [297] (7 mm cell size), with very similar electrostatic configuration and gas mixture. A better resolution is expected for the DCH, as a result of the longer drift distances and the employment of cluster timing techniques. Analytical calculations for the expected momentum, transverse momentum and angular resolutions, conservatively assuming a 100 µm point resolution, are plotted in the left panel of Fig. 7.9. The expected particle identification performance is presented in the right panel of Fig. 7.9. Results are

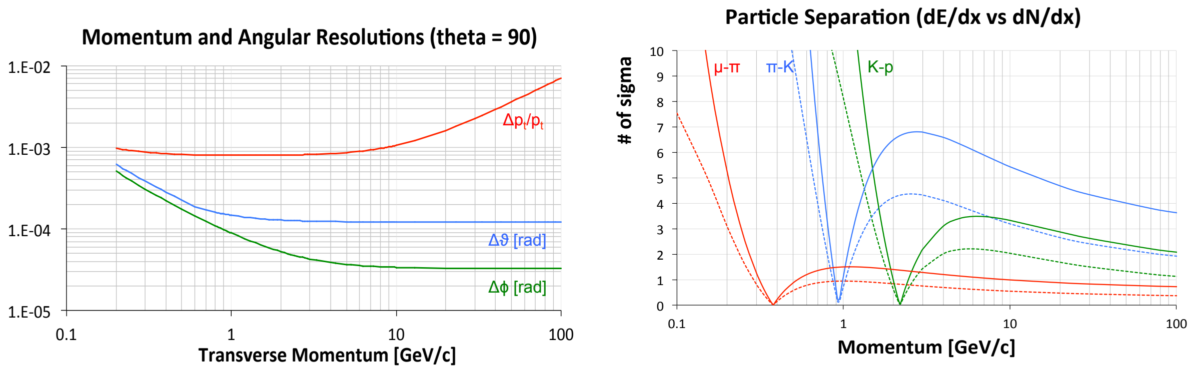

Figure 7.9: IDEA drift chamber performance. Left: Momentum and angular resolutions for $\theta = 90^\circ$ as a function of momentum; Right: Particle type separation in units of standard deviations as a function of momentum, with cluster counting (solid curves) and with dE/dx (dashed curves).

based on cluster counting, where it is assumed that the relative resolution on the measurement of the number of primary ionisation clusters ($N_{\rm cl}$) equals $1/\sqrt{N_{\rm cl}}$. For the whole range of momenta, particle separation with cluster counting outperforms the dE/dx technique by more than a factor of two. The expected pion/kaon separation is better than three standard deviations for all momenta except in a narrow range from 850 MeV to slightly above 1 GeV.

A layer of silicon micro-strip detectors surrounds the outside of the drift chamber providing an additional accurate space point as well as precisely defining the tracker acceptance.

7.4.3 IDEA Tracking System Performance

Simulations were performed to obtain a first estimate of the performance of the IDEA tracking system. In this study, a seven-layer cylindrical vertex detector, and a two-layer silicon wrapper, both with a $r\phi$ pitch of 20 µm , were placed inside and around the cylindrical drift chamber, respectively. Details of ionisation clustering for cluster counting/timing analysis were not simulated, so that the spatial resolution is conservatively limited to 100 µm. The results of this study, consolidated by those derived from a fast simulation, point to a transverse momentum resolution of $\sigma 1/p_{\rm T}) \simeq a \oplus b/p_{\rm T}$, with $a \simeq 3{\times}10^{-5}$ GeV^{-1} and $b \simeq 0.6 \times 10^{-3}$. The lightness of the drift chamber is reflected in the small multiple scattering b term. Correspondingly, an impact parameter resolution of $\sigma_{d_0} = a \oplus b/p \sin^{3/2}\theta$, with $a = 3$ µm and $b = 15$ µm GeV, is found. Lastly, angular resolutions of better than 0.1 mrad in both azimuthal and polar angle are demonstrated for tracks with momenta exceeding 10 GeV.

7.4.4 Backgrounds in the IDEA Tracking System

A GEANT4 simulation of the central parts of the IDEA detector has been implemented in the common software framework developed for the FCC experiments [298]. A study of the IPC background in the IDEA drift chamber was performed. Only very few of the primary $e^{\pm}$ particles have a transverse momentum large enough to reach the inner radius of the drift chamber starting (35 cm). The majority of the hits observed in the drift chamber are thus from secondary particles (mainly photons of energy below 1 MeV) produced by scattering off the material at lower radii. The average occupancy of the drift chamber due to this background was found to be 0.3% (3%) per bunch crossing at 91.2 (365) GeV, with a smooth decrease by a about a factor two from low to large radii. At the Z pole, a naive and very conservative integration over 20 bunch crossings – corresponding to the 400 ns maximum drift time – yields a maximum occupancy of about 10% in the inner-most drift cells. Based on experience from the MEG2 drift chamber, this occupancy, which allows over 100 hits to be recorded per track on average in the DCH, is deemed manageable.

Discussion in this meeting today

The level of occupancy is actually expected to be much smaller than this conservative estimate with the use of the drift chamber timing measurement. As opposed to charged particles that leave a string of ionisation in the drift cells they traverse, photons are characterised by a localised energy deposition. Signals from photons can therefore be effectively suppressed at the data acquisition level by requiring that at least three ionisation clusters appear within a time window of 50 ns. In addition, a charge string with a hole longer than 100 ns can be interpreted as two separate signals, as to avoid the integration of any remaining photon induced background over 20 bunch crossings, but rather over a time corresponding to only four bunch crossings. With this effective suppression of photon induced signals, the background from IPC is expected to remain low and to cause no adverse issues for the track reconstruction.

7.4.5 IDEA Preshower Detector

A preshower detector is located between the magnet and the calorimeter in the barrel region and between the drift chamber and the end-cap calorimeter in the forward region. In the barrel region, the magnet coil (Section 7.5) works as an absorber of about $1X_0$ and is followed by one layer of MPGD (Micro Pattern Gas Detector) chambers; a second layer of chambers follows after another $1X_0$ of lead. A similar construction occurs in the forward region, however, here with both absorber layers made from lead. The MPGD chamber layers provide an accurate determination of the impact point of both charged particles and photons, and therefore define the tracker acceptance volume with precision. They also further improve the tracking resolution. In addition, a large fraction of the π^0s can be tagged by having both photons from their decay identified by the preshower. The optimisation of the preshower system and the evaluation of its performance is in progress.

7.4.6 IDEA Dual-Readout Calorimeter

A lead-fibre dual-readout calorimeter [299] surrounds the second preshower layer. This calorimeter concept has been extensively studied and demonstrated over ten years of R&D by the DREAM/RD52 collaboration [300, 301]. The calorimeter is 2 m deep, which corresponds to approximately 7 λ_I. Two possible layouts have been implemented in the simulation for a realistic 4π detector. Both cover the full volume down to 100 mrad of the z axis, with no inactive region. In the first configuration, the calorimeter is made of truncated rectangular-base pyramidal towers with 92 different sizes. In the second, it is built with rectangular prisms coupled to pyramidal towers. The total number of fibres is of the order of 10^8 in both cases.

The dual-readout calorimeter is sensitive to the independent signals from scintillation light (S) and Čerenkov light (C) production, resulting in excellent energy resolution for both electromagnetic and hadron showers. By combining the two signals, the resolution estimated from GEANT4 simulations is found to be close to $10\%/\sqrt{E}$ for isolated electrons and $30\%/\sqrt{E}$ for isolated pions with negligible constant terms.

The dual-readout calorimeter provides very good intrinsic discrimination between muons, electrons/photons and hadrons for isolated particles [302]. Figure 7.10 demonstrates a nearly perfect separation in the C/S ratio for 80 GeV electrons and protons: for an electron efficiency of 98%, a simulated rejection factor of up to 600 can be reached for isolated protons. The rejection factor in jets remains to be evaluated experimentally. In addition to the C/S ratio, a few other variables, like the lateral shower profile, the starting time of the signal, and the charge-to-amplitude ratio, can be used to enhance the intrinsic calorimeter particle separation performance.

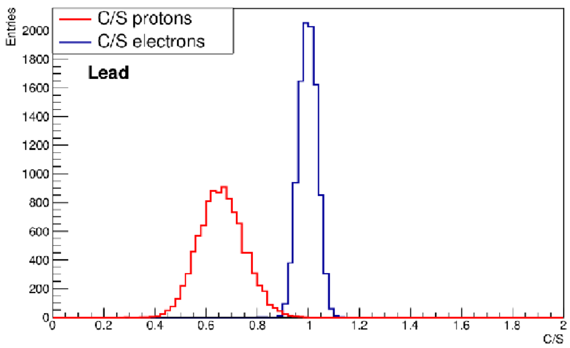

Figure 7.10: Particle identification performance of the dual-readout calorimeter: C/S ratio for 80 GeV isolated electrons and protons.

In addition to the intrinsic particle identification capabilities, the fine transverse granularity allows close showers to be separated and provides good matching to tracks in the inner, preshower signals, and muon tracks, making this calorimeter a good candidate for efficient particle-flow reconstruction. The need to disentangle signals produced by overlapping electromagnetic and hadron showers is likely to require longitudinal segmentation as well. Several ways to implement it were envisioned and are being studied, e.g., the classical division of the calorimeter in several compartments, an arrangement with fibres starting at different depths, the extended use of the timing information, etc. Each way has pros and cons and needs to be studied with both simulations and beam tests.

7.4.7 IDEA muon system

The muon system consists of layers of muon chambers embedded in the magnet return yoke. The area to be covered is substantial, which calls for a cost-effective chamber technology. Recent developments in the industrialisation of μ-Rwell-based large area chambers [303], proposed for the CMS detector phase-II upgrade, are promising.

7.5 Detector Magnet System

Both detector concepts, CLD and IDEA, employ a 2 T solenoidal field. In the case of CLD, the coil is situated outside the calorimeter system, as is the case for the detector designs considered in the linear collider studies. The larger tracker radius of CLD is compensated, in part, by a somewhat thinner hadron calorimeter and the coil has rather similar dimensions of 7.4 m length and 3.7 m inner radius. For the IDEA concept, a solution, similar to that of the ATLAS detector [304], is being pursued, in which a thin coil is placed inside the calorimeter system, where it functions as the first absorber layer of the preshower detector. Presently planned dimensions are a length of 6.0 m and an inner diameter of 4.2 m. With current technology, a radial thickness of 30 cm, including an effective Al thickness of 10 cm, looks feasible. At perpendicular incidence, this corresponds to a material thickness of $0.74X_0$ and $0.16\lambda_I$. Further R&D effort would be needed to pursue a more aggressive solution where the physical thickness as well as the material budget could be reduced to about 70% of these numbers.

A rewrite of this section has been promised by Herman Ten Kate

7.6 Constraints on readout systems

Number of channels, event size (dominated by backgrounds), trigger considerations, etc

TO BE WRITTEN BEFORE THE END OF JULY

7.7 Infrastructure Requirements

At the present conceptual design stage of the CLD and IDEA detectors, no engineering effort is available to assess the infrastructure needs of these experiments in detail. However, some preliminary requirements can be listed, based on the experience from CMS and on a first assessment made for the CLIC detectors [305, 306].

One may assume that sufficient capacity will be available for the equipment handling for installation and maintenance of the detectors due to the requirements of the much larger and heavier FCC-hh detectors. Similarly, the heating, ventilation and air-conditioning (HVAC) of the detector caverns is assumed to be covered by the requirements from FCC-hh.

The detector-specific power requirements have been documented in detail for the CMS experiment [306]. The total power needed for this experiment is about 3.5 MW. Since CLD and IDEA are of a similar size and complexity, the same total power needs can be assumed for each of these detectors. This estimate is very likely an upper limit, as the superconducting magnet systems in the FCC-ee detectors are operated at only 2 T, compared to 4 T at CMS and CLIC. The cryogenics and powering of the CMS magnet requires 0.9 MW of power.